Anomalous Hall Sensors with High Sensitivity and Stability Based on Interlayer Exchange-Coupled Magnetic Thin Films

Kang Wang[*,‡] Yiou Zhang[,‡] and Gang Xiao[†]

Department of Physics, Brown University, Providence, Rhode Island 02912, USA

In this work, we demonstrate that interlayer exchange-coupled magnetic thin films can be employed to fabricate ultrasensitive and thermally stable magnetic sensors, taking advantage of the linear anomalous Hall effect via tuning the interlayer exchange coupling and magnetic anisotropy. We investigate the magnetotransport and noise properties of these anomalous Hall sensors. The magnetic field detectability reaches $126.1\,\text{nT}/\sqrt{\text{Hz}}$ at 1 Hz and $4.5\,\text{nT}/\sqrt{\text{Hz}}$ at 1 kHz, at room temperature. Meanwhile, the achieved dynamic reserve is 103.0 dB. The magnetic field detectability shows a good temperature stability in the 200 to 300 K range. Within the temperature range, the temperature coefficient of sensitivity is determined to be 530 ppm/K. The high temperature stability is attributed to the interlayer exchange coupling, which also improves the stability against in-plane magnetic fields, beneficial for perpendicular magnetic field sensing. The interlayer exchange-coupled magnetic thin-film-based anomalous Hall sensors solve the trade-off between the sensor size, sensing capability, and stability, which are desirable for microimaging and biomedical applications.

I. INTRODUCTION

Magnetic sensors have been widely applied in industrial productions such as automotive applications [1] and read heads in data-storage devices [2,3]. In addition, magnetic sensors also have great potential in magnetic imaging [4], microscopy [5], and biomedical applications [6,7]. In these microsensing applications, the sensor size is one of the selection criteria for magnetic sensors. This is either because of the requirement of spatial resolution or because of the weak pointlike source. The anomalous Hall effect (AHE) in magnets is a good candidate for these magnetic sensing applications [8–12]. The AHE sensors can be fabricated with miniaturized sizes through simple fabrication procedures. In addition, the AHE sensors have superior properties including broad frequency response [13] and high sensitivity [9–11]. The sensitivity s, together with the intrinsic noise S_V, determines the magnetic sensing detectability $S_T^{0.5} = S_V^{0.5}/Is$, where I is the current applied to AHE sensors.

By tuning the perpendicular magnetic anisotropy to the spin-reorientation transition region, a linear anomalous Hall effect with the sensitivity as high as $10^4\,\boldsymbol{\Omega}/T$ can be achieved in single magnetic layer-based AHE sensors [Fig. 1(a)] [9–11]. Nevertheless, reaching such high sensitivity sacrifices temperature stability and the tolerance to

orthogonal magnetic fields [11]. Decreasing perpendicular anisotropy may enhance the stability, but also reduce the magnetic sensing capability [Fig. 1(b)] [12]. The trade-off between high sensitivity and stability of AHE sensors restrict applications in magnetic sensing that may be exposed to harsh environments.

In this work, we demonstrate that, interlayer exchange-coupled magnetic thin films can serve as a platform to fabricate high-performing AHE sensors with both high sensitivity and stability. In the magnetic multilayer structure, two magnetic layers are coupled through a nonmagnetic spacer between the two magnetic layers [14–20]. In addition to the perpendicular anisotropy, the interlayer exchange coupling (IEC) between the two magnetic layers provides an additional handle to control magnetizations and stability [Fig. 1(c)]. To get thorough insights into the performance of AHE sensors, we investigate the magnetotransport and noise properties of AHE sensors. Apart from sensitivity, investigations on the intrinsic noise offer additional insight into the performance of AHE sensors; however, few works have reported on it [8]. One expects that the AHE sensor possesses a low electronic noise that originates from thermal fluctuations of defects, because of its metallic feature. The noise power spectra density can be characterized by $\frac{S_V}{I^2 R^2} = \frac{\alpha}{Nf}$ where R is the resistance, N the number of charge carriers, f the frequency, and α the Hooge parameter [21–23]. On the other hand, the magnetic noise that originates from thermal magnetic fluctuations may vary depending on magnetic configurations, which also remains to be explored. Here we show that, by

---

*kang_wang@brown.edu
†gang_xiao@brown.edu
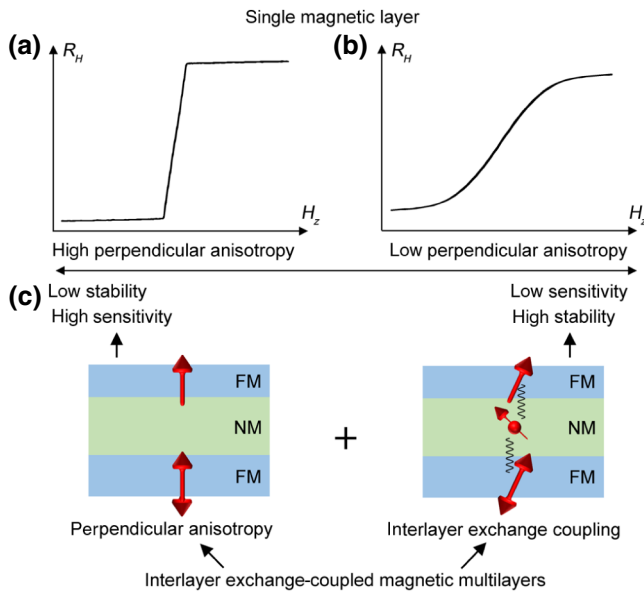‡These two authors contributed equally

FIG. 1. (a), (b) Sketches of anomalous Hall loops of a single magnetic layer-based anomalous Hall effect sensor with (a) a high perpendicular magnetic anisotropy and (b) a low perpendicular anisotropy (<0). R_H is the anomalous Hall resistance and H_z is the perpendicular magnetic field. The double-headed arrow represents the variation trend of the perpendicular anisotropy. For a single magnetic layer-based AHE sensor, increasing perpendicular anisotropy would induce a high sensitivity but also reduce the stability (left arrow). On the other hand, decreasing the perpendicular magnetic anisotropy would enhance the stability, but reduces the sensitivity (right arrow). (c) In an interlayer exchange-coupled magnetic multilayer structure, in addition to the perpendicular magnetic anisotropy that can be tuned to yield high sensitivity, the interlayer exchange coupling is present, which enhances the stability of AHE sensors. Red arrows are either localized spins in ferromagnetic layers or the itinerant spin in the nonmagnetic (NM) spacer. The red ball represents the conduction electron in the NM spacer. Wavy lines represent the conduction electron-mediated exchange interactions between localized spins in the two FM layers. The two FM layers are either ferromagnetically coupled or antiferromagnetically coupled, depending on the sign of the interlayer exchange coupling.

tuning the IEC and perpendicular anisotropy, when magnetizations are in the regions around the spin-reorientation transition and the transition from antiferromagnetic (AFM) to ferromagnetic (FM) coupling between the two magnetic layers, the AHE sensor has the best performance. The AHE sensors possess not only high sensitivity, low intrinsic noise, but also high temperature stability and the tolerance to orthogonal magnetic fields. The microsized AHE sensors with both high sensitivity and stability are possible to apply in microsensing such as detection of magnetically labeled biomolecules and magnetic imaging, under wide-ranging environmental conditions.

II. SAMPLE PREPARATION AND EXPERIMENTAL METHODS

To fabricate high-performing AHE sensors with optimized properties, we deposit multilayers of $MgO(1.6)/Co_{40}Fe_{40}B_{20}(t_1)/Ta(t_{Ta})/Co_{40}Fe_{40}B_{20}(t_2)/MgO(1.6)/TaO_x(1.0)$ (layer thicknesses in nanometers) on thermally oxidized silicon wafers using a high-vacuum magnetron sputtering system. The cross-section schematic view of the multilayer stack is presented in Fig. 2(a). The total thickness of the top and bottom ferromagnetic layers is fixed to be 1.8 nm ($t_1 = 0.8$, 0.9 and 1.0 nm). The Ta-layer thickness t_{Ta} varies from 0.6 to 1.4 nm. We use photolithography and ion milling to pattern multilayers into Hall crosses. The SEM image of a Hall cross is presented in Fig. 2(b). The active area of the Hall cross is $20 \times 20 \, \mu m^2$. In order to reduce the Johnson noise that shows a positive correlation with the resistance between two Hall voltage leads, we deposited Cr/Au layers as electrodes. We then perform the postgrowth thermal annealing in a high-vacuum chamber at different temperatures for 1 h, while applying a perpendicular magnetic field of approximately 0.4 T. Varying layer thicknesses and annealing temperatures allows us to get insight into the performance of AHE sensors with different magnetic configurations. As a comparison, we also deposit $Ta(1.6)/Co_{40}Fe_{40}B_{20}(0.9)/MgO(1.6)/TaO_x(1.0)$ on thermally oxidized silicon wafers. The sensing mode of the single $Co_{40}Fe_{40}B_{20}$ layer-based AHE sensor is achieved by annealing samples at a moderate temperature.

To obtain the accurate estimation of the sensitivity of AHE sensors, we use a coil to generate ac perpendicular
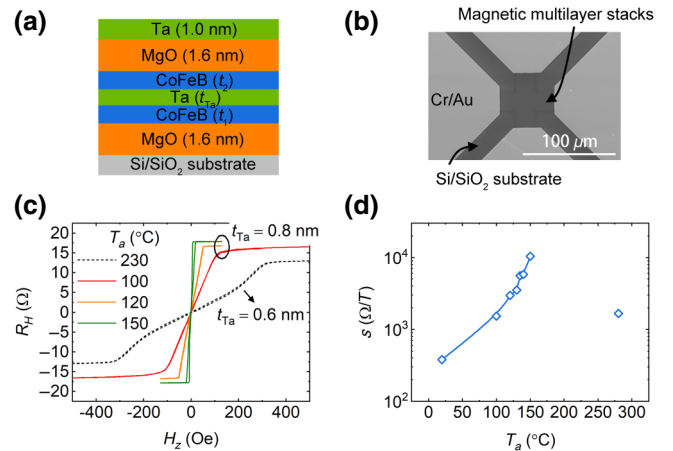

FIG. 2. (a) Cross-section schematic view of the multilayer stack. (b) SEM image of a Hall cross. The active area of the Hall cross is $20 \times 20 \, \mu m^2$. (c) Anomalous Hall resistance (R_H) versus perpendicular magnetic field (H_z) for magnetic multilayers with $t_{Ta} = 0.6$ nm (dashed, $t_1 = 0.9$ nm) and 0.8 nm (solid, $t_1 = 1.0$ nm). Samples are annealed in a high-vacuum chamber at different annealing temperatures T_a for 1 h. (d) Anomalous Hall sensitivity of magnetic multilayers with $t_{Ta} = 0.8$ nm, as a function of the annealing temperature.

magnetic field $\Delta H_z \sin(2\pi\omega t)$, while applying a constant perpendicular field H_z through the superconducting coil in the Quantum Design® Physical Property Measurement System (PPMS). The frequency $2\pi\omega = 5$ Hz and $\Delta H_z = 0.3$ Oe. The sensitivity $s = \frac{\Delta R_H}{\Delta H_z}$ at the field H_z is then derived by measuring the corresponding anomalous Hall voltage response that gives the anomalous Hall resistance $R_H + \Delta R_H \sin(\omega t)$. The ac measurement gives a more accurate estimation of the sensitivity value, while the value derived from the slope of Hall loops may be overestimated since a small coercivity may affect the actual values of the sensitivity [24,25].

Noise measurements are also performed in the PPMS. The block diagram of the noise measurement system can be found in our previous work [26]. Briefly, we use a current source to apply 1-mA current to the AHE sensor; the ac output from two Hall voltage leads is amplified by two low-noise preamplifiers in the PPMS chamber and then further amplified outside the chamber. The noise from amplifiers is cancelled out through a cross-correlation method [27]. Accurate measurements of the anomalous Hall sensitivity and the intrinsic noise together characterize the performance of AHE sensors.

III. MAGNETIC PROPERTIES

We first show magnetic properties of interlayer exchange-coupled magnetic thin films by tuning the IEC and magnetic anisotropies. Figure 2(c) shows anomalous Hall loops of magnetic multilayers with $t_{Ta} = 0.6$ and 0.8 nm. For the multilayer structure with $t_{Ta} = 0.6$ nm, a nonlinear and reversible anomalous Hall loop is observed. This infers that the two ferromagnetic layers are antiferromagnetically coupled [18,20]. The AFM coupling induces a low sensitivity (347 Ω/T) at zero magnetic field. The AFM coupling changes into FM coupling when t_{Ta} changes from 0.6 to 0.8 nm. The FM coupling is followed by the other transition into the AFM coupling when further increasing t_{Ta} to 1.2 nm (not shown here). Both the sign and strength of the IEC oscillate periodically, which is attributed to the presence of Friedel-like spatial oscillations in spin density in the Ta spacer [16].

For the multilayer structure with $t_{Ta} = 0.8$ nm, the perpendicular magnetic anisotropy increases when increasing the annealing temperature T_a from 100 to 150 °C [Fig. 2(c)]. The increase in perpendicular anisotropy gives rise to a higher sensitivity, as shown in Fig. 2(d), but also promotes the emergence of the multidomain state. The multidomains would increase the magnetic noise that is undesirable for magnetic sensing applications. The competition between the sensitivity and magnetic noise motivates us to perform magnetotransport and noise measurements of SAFs with different magnetic anisotropies. In the following text, we show experimental results of magnetic multilayers with $t_{Ta} = 0.8$ nm, while the multilayers with

other Ta-spacer thicknesses possess lower magnetic sensing detectability, as discussed later.

IV. MAGNETOTRANSPORT AND NOISE PROPERTIES OF AHE SENSORS

We focus on three samples with different perpendicular magnetic anisotropies. We denote three samples as "sample1," "sample2," and "sample3," respectively. All three samples have a Ta-spacer thickness t_{Ta} of 0.8 nm. Sample1 has magnetic layer thickness $t_1 = 0.8$ nm ($t_2 = 1.0$ nm), while sample2 and sample3 have magnetic layer thicknesses $t_1 = t_2 = 0.9$ nm. We anneal sample1 and sample2 at an annealing temperature of 120 °C. Sample3 is annealed at a higher annealing temperature of 140 °C. Figure 3(a) shows anomalous Hall loops of the three samples. The anomalous Hall loop of sample3 shows an irreversible feature near the saturation field. This is a typical feature of the presence of the multidomain state [28]. The linear anomalous Hall loops of sample1 and sample2 suggest that magnetizations of the two samples are in the region around the spin-reorientation transition.

As an essential parameter to characterize the performance of AHE sensors, the sensitivity is presented in Fig. 3(b). The sensitivity increases with increasing the perpendicular anisotropy, and reaches 8634 Ω/T for sample3. The sensitivity value is comparable with that of the single magnetic layer-based AHE sensors [9,10]. We determine the dynamic range $2H_{DRg}$ to be the same as the full width at half maximum of the H_z dependence of the sensitivity. The dynamic range of sample1 that has the lowest perpendicular anisotropy is 197 Oe, while sample2 and sample3 with larger perpendicular anisotropies have lower dynamic ranges of 111 and 33 Oe, respectively.

Apart from the sensitivity, noise spectra are also measured, as shown in Fig. 3(c). The H_z-dependent noise S_V at 1 Hz is derived from noise spectra and plotted in Fig. 3(d). The noise spectrum includes $1/f$ noise and white noise. The $1/f$ noise that is dominant at low-frequency originates from both the thermal fluctuations of defects and thermal magnetic fluctuations. In the sensing region, $1/f$ noise increases with increasing the perpendicular anisotropy [Fig. 3(d)]. This is because of enhanced thermal magnetic fluctuations with the emergence of the multidomain state. For sample1, the noise in the sensing region is the same as the noise in the saturation region [Fig. 3(d)]. This implies that the magnetic $1/f$ noise is not as large as the defect-induced electronic $1/f$ noise.

The magnetic sensing detectability is calculated through $S_T^{0.5} = S_V^{0.5}/Is$, which is plotted in Fig. 3(e). The best field detectability is achieved in sample2 (60.4 nT/$\sqrt{Hz}$ at 1 Hz) at the bias field $H_B = 44$ Oe. The field detectability is better than the detectability of conventional semiconductor Hall sensors (μT/$\sqrt{Hz}$ at 1 Hz) by two orders of magnitude [8,29]. On the one hand, the anomalous Hall
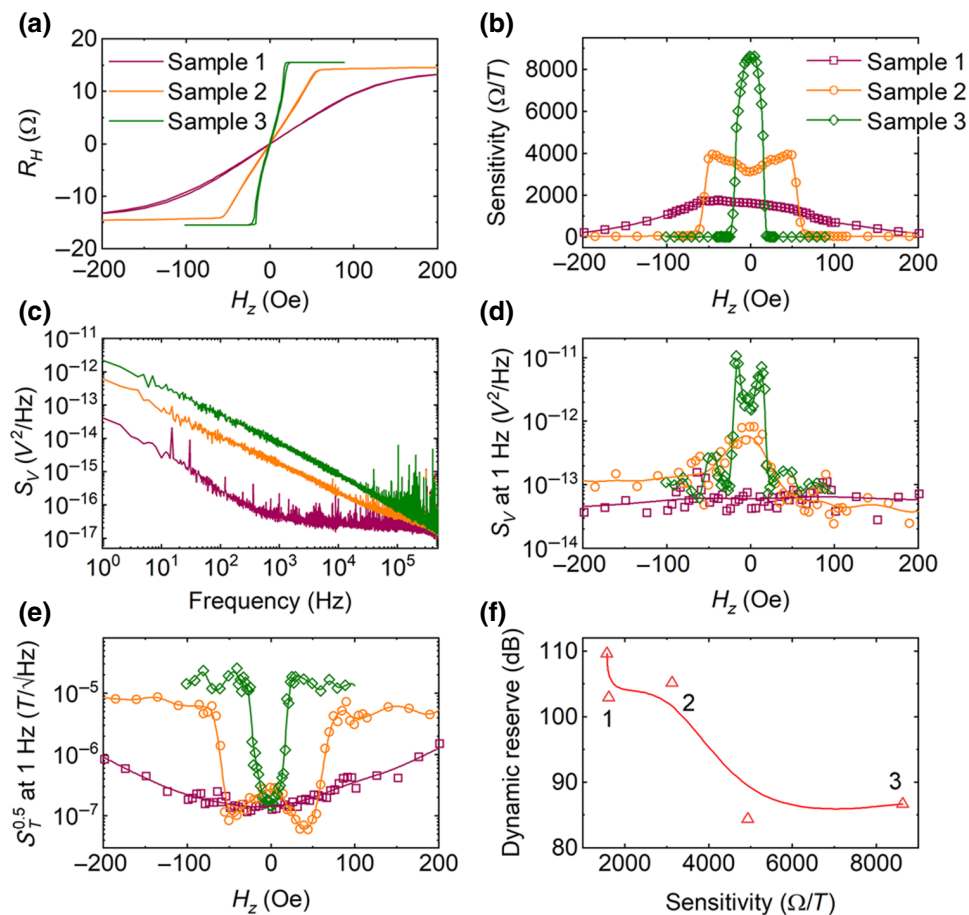
FIG. 3. (a) Anomalous Hall loops of three magnetic multilayers with different perpendicular anisotropies. Sample1 has the magnetic layer thickness $t_1 = 0.8$ nm ($t_2 = 1.0$ nm), while sample2 and sample3 have the magnetic layer thicknesses $t_1 = t_2 = 0.9$ nm. (b) The anomalous Hall sensitivity measured at different perpendicular magnetic field H_z. (c) Noise spectra for three samples measured at zero magnetic field. (d) The intrinsic noise, and (e) magnetic field detectability at 1 Hz as a function of H_z. (f) The dynamic reserve for three samples and the other two samples with similar structures.

sensitivity is larger than the sensitivity of conventional semiconductor Hall sensors by one order of magnitude [29–31]. On the other hand, the AHE sensor possesses a lower noise compared with semiconductor Hall sensors that suffer from semiconductor limitations [8,29]. At zero field, sample1 has the best field detectability (126.1 nT/$\sqrt{\text{Hz}}$ at 1 Hz) among all three samples, and the detectability reaches 4.5 nT/$\sqrt{\text{Hz}}$ at 1 kHz. The high detectability of sample1 is attributed to the low magnetic noise, although it has the lowest sensitivity among all three samples.

To quantify the performance of AHE sensors, we calculate the dynamic reserve that is defined as DRs $= 20 \log_{10}[2H_{\text{DRg}}/S_T^{0.5} (\text{at 1 Hz})]$, as presented in Fig. 3(f). For high-performing magnetic sensors, a large dynamic reserve is expected. Figure 3(f) shows that the dynamic reserve decreases with increasing the perpendicular anisotropy (sensitivity), for all three samples and the other two samples with similar structures. Sample1 that has the best detectability at zero field has the dynamic reserve of 103.0 dB. In our previous work, we measured that a commercial semiconductor Hall sensor (Lakeshore Model HGT-2101) has a detectability of 7 μT/$\sqrt{\text{Hz}}$ at 1 Hz, under 1 mA of input current [8]. Although semiconductor Hall sensors have much larger dynamic ranges (1 T),

the dynamic reserve is determined to be 103.0 dB, which is comparable with our AHE sensors. Large dynamic reserves of our AHE sensors allow for accurate measurement of the magnetic field even in the presence of the strong background magnetic field.

Further decreasing the perpendicular anisotropy may increase the dynamic range, but would also reduce the sensing capability, which is undesirable for magnetic sensing. The characterization results of three samples are presented in Table I. By tuning the perpendicular anisotropy to the spin-reorientation transition region, one expects to fabricate AHE sensors with high detectability.

V. TEMPERATURE STABILITY OF AHE SENSORS

We perform transport and noise measurements of the interlayer exchange-coupled magnetic thin films at different temperatures T, to investigate temperature stability of AHE sensors. Figure 4(a) shows anomalous Hall loops of sample1 that are measured at 300, 250, 200, and 150 K, respectively. The anomalous Hall loop shows a much weaker temperature dependence compared with the single magnetic layer-based AHE sensors [11,12,32]. This is what we expect as a result of the IEC in the multilayer structure. For sample1, both the saturation magnetization

TABLE I. Sensitivity s at zero field, dynamic range DRg, the best magnetic sensing detectability ($S_T^{0.5}$) at 1 Hz, the bias field H_B under which the best field detectability is observed, dynamic reserve DRs and temperature coefficient of sensitivity α_s of sample1, sample2, and sample3 with different perpendicular magnetic anisotropies. Sensitivity, dynamic range, detectability, bias field, and dynamic reserve are measured at 300 K. The temperature coefficients of sensitivity are calculated within the temperature range from 300 to 200 K.

	$s(\Omega/T)$	DRg(Oe)	$S_T^{0.5}$ at 1 Hz(nT/$\sqrt{Hz}$)	H_B(Oe)	DRs(dB)	α_s(ppm/K)
Sample1	1622	197	126.1	0	103.0	530
Sample2	4933	111	60.4	44	105.2	4060
Sample3	8634	33	143.8	0	86.7	6800

and coercivity increase with decreasing the temperature. The increase in coercivity is most probably due to the enhanced perpendicular anisotropy, as well as because of suppressed thermal fluctuations of magnetization across the field-induced magnetization switching [32–34]. The slope of the anomalous Hall loop increases with decreasing the temperature. However, the temperature-dependent coercivity induces that the sensitivity increases slightly when decreasing the temperature from 300 to 200 K, and then drops with further decreasing the temperature to 150 K, as presented in Fig. 4(b). Similar to the temperature-dependent sensitivity, in the sensing region, the intrinsic noise (at 1 Hz) shows ignorable variations

within the temperature range from 300 to 200 K, and then increases with decreasing the temperature to 150 K, as presented in Fig. 4(c). In the saturation region, the intrinsic noise decreases with decreasing the temperature. This is expected from the suppressed Johnson noise. The magnetic sensing detectability is calculated and plotted in Fig. 4(d). It is noteworthy that the field detectability data measured at $T = 300$, 250, and 200 K collapse in the sensing region. The detectability increases to approximately 250 nT/$\sqrt{Hz}$ at 1 Hz when decreasing the temperature to 150 K. Both the nearly unchanged sensitivity and detectability suggest that sample1 has a good temperature stability in the 300 to 200 K range.
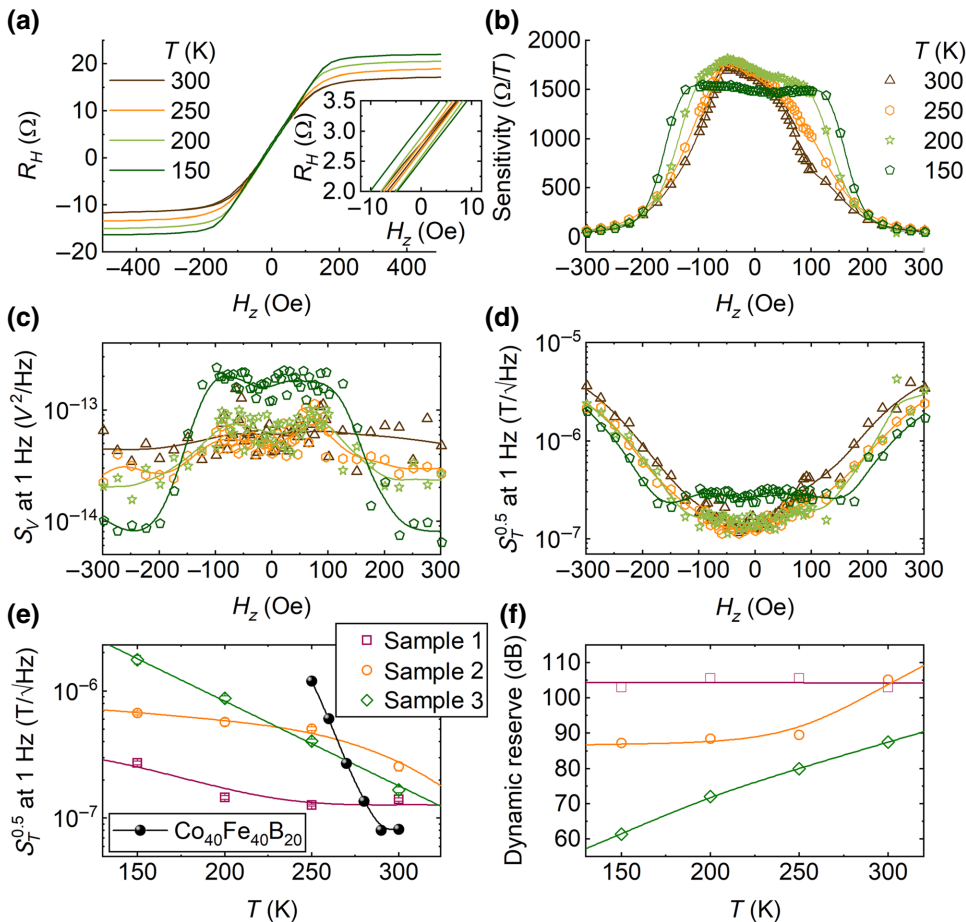

FIG. 4. (a) Anomalous Hall loops of sample1 that are measured at 300, 250, 200, and 150 K, respectively. The insert shows the enlarged figure. (b) Anomalous Hall sensitivity, (c) the intrinsic noise, and (d) magnetic sensing detectability of sample1 measured at different temperatures. (e) The field detectability and (f) dynamic reserve of three samples as a function of temperature. In (e), the field detectability of the single $Co_{40}Fe_{40}B_{20}$ layer-based AHE sensor is also presented. The field detectability of the single-layer system is recorded at a bias field of -14 Oe at which the field detectability value is the lowest.

We also perform magnetotransport and noise measurements of sample2 and sample3 at different temperatures. We plot the temperature-dependent field detectability (at zero field and 1 Hz) and dynamic reserve, for all three samples, in Figs. 4(e) and 4(f), respectively. Sample1 that has the best detectability at zero field, also has the best temperature stability among all three samples. We use a temperature coefficient of sensitivity α_s that is defined as $|\Delta s/s\Delta T|$ to quantify temperature stability. The temperature coefficients for sample1, sample2, and sample3 are 530, 4060, and 6800 ppm/K, respectively, within the temperature range from 300 to 200 K. The temperature coefficient of sensitivity (530 ppm/K for sample1) has the same order of magnitude as the temperature coefficient of conventional semiconductor Hall sensors. However, in semiconductor Hall sensors, reaching such a low temperature coefficient requires sacrificing the sensitivity ($<$ $10^2\,\Omega/T$) [30,31]. Our results suggest that the interlayer exchange-coupled magnetic thin-film-based AHE sensors outperform semiconductor Hall sensors in sensitivity, field detectability, and temperature stability.

As a comparison, we also measure magnetotransport and noise properties of the single $Co_{40}Fe_{40}B_{20}$ layer-based AHE sensor in the 310 to 250 K range. The temperature-dependent magnetic field detectability at 1 Hz at a bias field $H_B = -14$ Oe (at which the field detectability value is lowest) is also presented in Fig. 4(e). The experimental results show that the field detectability of the single $Co_{40}Fe_{40}B_{20}$ layer system has a stronger temperature dependence, compared with the interlayer exchange-coupled magnetic multilayer structure. We also calculate the temperature coefficient of sensitivity of the single $Co_{40}Fe_{40}B_{20}$ layer-based AHE sensor. The temperature coefficient α_s is calculated to be 6540 ppm/K within the temperature range from 310 to 250 K. This value is much larger than the temperature coefficient of sensitivity (530 ppm/K) of sample1, which is calculated in the 300 to 200 K range. The experimental results confirm that the interlayer exchange-coupled magnetic multilayer structure has a better temperature stability compared with the single $Co_{40}Fe_{40}B_{20}$ layer-based AHE sensor, as a result of the IEC in the multilayer structure.

VI. STABILITY AGAINST ORTHOGONAL MAGNETIC FIELDS

In addition to the temperature stability, reaching high tolerance to orthogonal magnetic fields is essential as well for AHE sensors in applications of perpendicular magnetic field sensing. The IEC in magnetic multilayers is expected to enhance the stability. To confirm this, we measure anomalous Hall loops of the interlayer exchange-coupled system and the single $Co_{40}Fe_{40}B_{20}$ layer system, while applying an in-plane magnetic field $\mathbf{H_{IP}}$. $\mathbf{H_{IP}}$ is applied either parallel ($\alpha = 0°$) or perpendicular ($\alpha = 90°$) to the
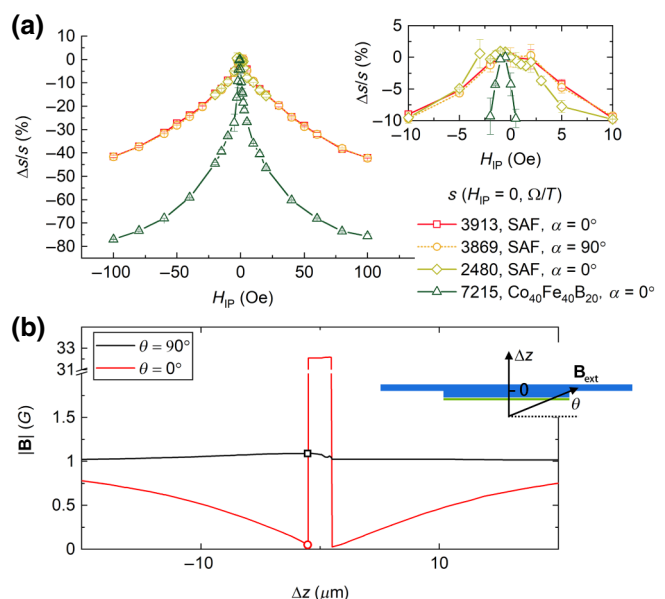

FIG. 5. (a) Relative changes ($\Delta s/s$) of the anomalous Hall sensitivity as a function of in-plane magnetic field H_{IP}. The ($\Delta s/s$) is derived from the slope of anomalous Hall loops of magnetic multilayers with different $s(H_{IP} = 0)$. We also plot ($\Delta s/s$) for a single $Co_{40}Fe_{40}B_{20}$ layer system (green). $\alpha = 0°$ and $\alpha = 90°$ respectively represent that the $\mathbf{H_{IP}}$ is applied parallel and perpendicular to the current flow direction. The insert is the partial enlarged figure. Error bars are derived from multiple measurements. (b) The magnetic field ($|\mathbf{B}|$) along Δz axis that passes through the center of the magnetic flux concentrator. The insert shows the schematic depiction of the MFC on an AHE sensor. θ is the angle between the external magnetic field $\mathbf{B_{ext}}$ and the sample plane. In simulations, we apply $\mathbf{B_{ext}} = 1$ G, parallel ($\theta = 0°$, red), or perpendicular ($\theta = 90°$, black) to the sample plane. Dots are the data at $\Delta z = -1.05\,\mu m$ that is near the position of the AHE sensor.

current flow direction. Figure 5(a) shows that the relative changes $\Delta s/s = [s(H_{IP}) - s(H_{IP} = 0)]/s(H_{IP} = 0)$ of the sensitivity increases with increasing $|H_{IP}|$, but is independent of the in-plane field direction and the perpendicular magnetic anisotropy that determines $s(H_{IP} = 0)$. We use the value of $|\Delta s/s|$ to characterize the cross-field error. The interlayer exchange-coupled system shows a lower cross-field error compared with the single $Co_{40}Fe_{40}B_{20}$ layer system. In particular, when $|H_{IP}| < 2$ Oe, as shown in the insert in Fig. 5(a), the $\Delta s/s$ keeps at about 0% for interlayer exchange-coupled magnetic thin films, while it changes by almost 10% for the single $Co_{40}Fe_{40}B_{20}$ layer system.

Magnetic flux concentrator (MFC) can be employed to amplify external magnetic fields [35–37]. Here we propose that by depositing a MFC on the top of the AHE sensor, the stability against in-plane magnetic fields can be further improved. We use the COMSOL Multiphysics® to preliminarily investigate the MFC's effect on magnetic fields.

The setup comprises two cuboids with dimensions of $20 \times 20 \times 1$ and $40 \times 40 \times 1$ μm^3, respectively, as shown in the insert in Fig. 5(b). The parameters we adopt in simulations are the same as parameters of $Co_{88}Zr_4Nb_8$ materials. The relative permeability is 857 and the relative permittivity is 1. As shown in Fig. 5(b), the MFC suppresses the in-plane magnetic field by almost 30 times near the MFC's surface, while there is only a slight amplification of the perpendicular magnetic field. The high-quality MFC can be deposited by magnetron sputtering, which has been demonstrated in our previous work [36]. The MFC, together with the interlayer exchange coupling in the AHE sensor can promote high stability of the AHE sensor against in-plane magnetic fields. The high temperature stability and tolerance to in-plane magnetic fields make AHE sensors highly promising in microsensing applications under wide-ranging environmental conditions.

VII. DISCUSSIONS

We demonstrate that the interlayer exchange-coupled magnetic thin-film-based AHE sensor has an outstanding performance with both high sensitivity and stability. We summarize our characterization results of sample1, sample2, and sample3 in Table I. To achieve the best performance of AHE sensors, we also perform transport and noise measurements of magnetic multilayers with different magnetic layer thicknesses and t_{Ta}. Magnetic layer thicknesses ($t_1 = 0.8$, 0.9, and 1.0 nm) have ignorable influences on the performance of AHE sensors. The t_{Ta} controls the IEC sign and strength. In multilayers with the smaller t_{Ta} (0.6 and 0.7 nm), the two magnetic layers are antiferromagnetically coupled. This gives rise to the low sensitivity around zero magnetic field, as shown in Fig. 2(c). In multilayers with the larger t_{Ta} (0.9 and 1.0 nm), the two magnetic layers are strongly ferromagnetically coupled. In this scenario, a higher sensitivity is present; however, the intrinsic noise is also large because of the finite coercivity. This gives rise to a large value of the field detectability. We summarize characterization results of multilayers with different t_{Ta} in Table II. Our experimental results suggest that sample1 with $t_{Ta} = 0.8$ nm has the best performance among all the samples. This is because magnetizations are in the spin-reorientation transition region, as well as possibly because of the weak IEC strength in the vicinity of the transition from AFM coupling to FM coupling between the two ferromagnetic layers. Nevertheless, in the IEC transition region, whether multilayers with FM coupling or AFM coupling have a better performance remains to be further studied through fabricating multilayers with smaller changes in t_{Ta}.

The anomalous Hall angle $\theta_{AHE} = \rho_H/\rho_{xx}$ is calculated to characterize the efficiency of AHE sensors. ρ_H is the anomalous Hall resistivity, and ρ_{xx} is the longitudinal resistivity. For the interlayer exchange-coupled magnetic

TABLE II. Sensitivity s at zero field, the best magnetic sensing detectability ($S_T^{0.5}$) at 1 Hz, the bias field H_B under which the best field detectability is observed, of multilayer systems with different Ta-spacer thicknesses t_{Ta}. All parameters are measured at 300 K. The characterization results of the multilayer structure with $t_{Ta} = 0.8$ nm is that of sample1.

t_{Ta}(nm)	IEC	$s(\Omega/T)$	$S_T^{0.5}$ at 1 Hz $(nT/\sqrt{Hz})$	H_B(Oe)
0.6	AFM	347	539.1	0
0.7	AFM	589	417.7	0
0.8	Weak FM	1622	126.1	0
0.9	FM	3181	551.5	26.9
1.0	FM	5553	397.1	10.3

thin films of $Co_{40}Fe_{40}B_{20}/Ta/Co_{40}Fe_{40}B_{20}$, the anomalous Hall angle is determined to be approximately 0.7%. One expects that, by replacing $Co_{40}Fe_{40}B_{20}$ with other magnets, such as FePt [11,12], with larger anomalous Hall angles, the efficiency of AHE sensors can be improved. AHE sensors with different material compositions remain to be explored.

Among magnetic sensors with miniaturized sizes, besides Hall sensors, the giant magnetoresistance (GMR) sensor and tunneling magnetoresistance (TMR) sensor have also been attracting great interest [26,35–37]. MR sensors have a better field detectability than our AHE sensors. Nevertheless, both GMR and TMR sensors are fabricated with much more complex fabrication processes. The GMR sensor performs with a high power consumption. A better magnetic sensing detectability can be achieved in TMR sensors based on magnetic tunnel junctions (MTJs) [26,36,37]. However, TMR sensors usually suffer from large $1/f$ noise, which scales inversely with junction areas and limits its performance with small size. In a TMR sensor with superparamagnetic free layer, the achieved magnetic field detectability is $40 \, nT/\sqrt{Hz}$ at 1 Hz [26], one third of that of the AHE sensor in this work, yet the sensing area is 14 times larger. We present a summary of magnetic field detectability and sensing areas of some MR sensors [8,37–40] in Table III. In Table III, we also show the calculation results of possible field detectability of MR sensors when considering the reduction in the sensing area of MR sensors to the same as the sensing area of our AHE sensors ($400 \, \mu m^2$). In calculations, we take into consideration that the intrinsic voltage noise scales inversely with junction areas and assume that the sensitivity is independent of junction areas of MR sensors. According to the data in Table III, we can conclude that if the same sensing area is used, one may expect that the AHE sensor performs comparably or even outperforms TMR sensors in microsensing.

MFCs are generally used to improve the sensitivity thus to improve the field detectability of GMR and TMR sensors [35–37]. One expects that the visible amplifications

TABLE III. Sensing area and magnetic field detectability of our AHE sensors and MR sensors in different references (Ref. No.). The kind of sensitive element (GMR or TMR) that is used is also shown. We also calculate the possible field detectability of MR sensors if considering the reduction in sensing area to the same as the sensing area of our AHE sensors. In this calculations, we take into consideration that the intrinsic voltage noise scales inversely with junction areas and assume the sensitivity is independent of junction areas of MR sensors. All these results are measured without MFCs.

Ref. No.	Sensitive element	Sensing area (μm^2)	$S_T^{0.5}$ (nT/$\sqrt{}$Hz)	Estimated $S_T^{0.5}$ (nT/$\sqrt{}$Hz) with reduced sensing area
In our work	AHE	400	126 at 1 Hz; 4.5 at 1 kHz	126 at 1 Hz; 4.5 at 1 kHz
[40]	TMR	250 000	16.2 at 1 Hz; 0.219 at high frequency	10125 at 1 Hz; 136.9 at 1 kHz
[39]	TMR	1500	1.8 at 10 Hz	6.75 at 10 Hz
[38]	TMR	11 020 000	0.115 at 196 Hz	3168.25 at 196 Hz
[37]	TMR	2 380 000	0.455 at 100 Hz	2707.25 at 100 Hz
[8]	TMR	5655	40 at 1 Hz	565.5 at 1 Hz

of the perpendicular magnetic field can also be achieved through optimizing the geometry and material properties of the MFC, although the amplification may not be as large as that achieved for MR sensors. Moreover, GMR and TMR sensors are generally used for in-plane magnetic field sensing [26,35,36]. If combing AHE sensors and GMR or TMR sensors together, one may expect to detect three-dimensional magnetic field with high field resolution.

VIII. CONCLUSION

We succeed in fabricating high-performing AHE sensors with both high sensitivity and stability, exploiting the magnetic multilayers of $Co_{40}Fe_{40}B_{20}/Ta/Co_{40}Fe_{40}B_{20}$. We perform magnetotransport and noise measurements to characterize the magnetic sensing capability of AHE sensors. The AHE sensor has the best performance when magnetizations are tuned to the regions around the spin-reorientation transition and the transition from AFM coupling to FM coupling between the two ferromagnetic layers. The AHE sensor that has the best performance has a multilayer structure comprising a Ta spacer with a spacer thickness of 0.8 nm, two $Co_{40}Fe_{40}B_{20}$ layers that sandwich the Ta spacer, and two MgO layers that sandwich the tri-layer structure including the two $Co_{40}Fe_{40}B_{20}$ layers and the Ta spacer. At room temperature, the anomalous Hall sensitivity is $1622\,\Omega/T$. The magnetic sensing detectability reaches 126.1 nT/$\sqrt{}$Hz at 1 Hz and 4.5 nT/$\sqrt{}$Hz at 1 kHz. The AHE sensor also has a large dynamic range of 197 Oe and a large dynamic reserve of 103.0 dB. The AHE sensor outperforms the conventional semiconductor Hall sensors in both sensitivity and detectability. Temperature-dependent studies are conducted. Benefiting from the IEC in the multilayer structure, the AHE sensor has a low-temperature coefficient of sensitivity of 530 ppm/K in the 200 to 300 K range. The IEC also improves the tolerance of AHE sensors to orthogonal magnetic fields. The high stability against both temperature and in-plane magnetic fields allows AHE sensors to be applied in magnetic

sensing under wide-ranging environmental conditions. The high-performing AHE sensors with miniaturized sizes have great potential in applications of microsensing such as detection of biomolecules and magnetic imaging. We expect that, by optimizing lateral structures of AHE sensors, material compositions and integrating with MFCs with optimized materials, sizes, and geometries, better performing AHE sensors with better detectability and higher stability can be fabricated.

ACKNOWLEDMENTS

[1] C. Treutler, Magnetic sensors for automotive applications, Sens. Actuators, A Phys. **91**, 2 (2001).

[2] J. M. Daughton, GMR and SDT sensor applications, IEEE Trans. Magn. **36**, 2773 (2000).

[3] P. P. Freitas, S. Cardoso, R. Sousa, W. Ku, R. Ferreira, V. Chu, and J. P. Conde, Spin dependent tunnel junctions for memory and read-head applications, IEEE Trans. Magn. **36**, 2796 (2000).

[4] C. Smith, R. Schneider, T. Dogaru, and S. Smith, Eddy-Current testing with GMR magnetic sensor arrays, AIP Conf. Proc. **700**, 406 (2004).

[5] E. A. Lima, A. C. Bruno, H. R. Carvalho, and B. P. Weiss, Scanning magnetic tunnel junction microscope for high-resolution imaging of remanent magnetization fields, Meas. Sci. Technol. **25**, 105401 (2014).

[6] S. G. Grancharov, H. Zeng, S. Sun, S. X. Wang, S. O'Brien, C. Murray, J. Kirtley, and G. Held, Bio-functionalization of monodisperse magnetic nanoparticles and their use as biomolecular labels in a magnetic tunnel junction based sensor, J. Phys. Chem. B **109**, 13030 (2005).

[7] P. Manandhar, K.-S. Chen, K. Aledealat, G. Mihajlović, C. S. Yun, M. Field, G. J. Sullivan, G. F. Strouse, P. B. Chase, and S. von Molnár, The detection of specific biomolecular interactions with micro-Hall magnetic sensors, Nanotechnology **20**, 355501 (2009).

[8] Y. Zhang, Q. Hao, and G. Xiao, Low-Frequency noise of magnetic sensors based on the anomalous hall effect in Fe–Pt alloys, Sensors **19,** 3537 (2019).

[9] G. Yang, Y. Li, X. Chen, J. Zhang, and G. Yu, Ultrasensitive anomalous Hall effect in Ta/CoFe/oxide/Ta multilayers, Adv. Condens. Matter Phys. **2016,** 9734610 (2016).

[10] T. Zhu, P. Chen, Q. Zhang, R. Yu, and B. Liu, Giant linear anomalous Hall effect in the perpendicular CoFeB thin films, Appl. Phys. Lett. **104,** 202404 (2014).

[11] Y. Lu, J. Cai, H. Pan, and L. Sun, Ultrasensitive anomalous Hall effect in $SiO_2/Fe\text{-}Pt/SiO_2$ sandwich structure films, Appl. Phys. Lett. **100,** 022404 (2012).

[12] Q. Hao, W. Chen, S. Wang, and G. Xiao, Anomalous Hall effect and magnetic properties of $FexPt_{100-x}$ alloys with strong spin-orbit interaction, J. Appl. Phys. **122,** 033901 (2017).

[13] I. Fergen, K. Seemann, A. Weth, and A. Schüppen, Soft ferromagnetic thin films for high frequency applications, J. Magn. Magn. Mater. **242,** 146 (2002).

[14] R. Duine, K.-J. Lee, S. S. Parkin, and M. D. Stiles, Synthetic antiferromagnetic spintronics, Nat. Phys. **14,** 217 (2018).

[15] P. Grünberg, R. Schreiber, Y. Pang, M. Brodsky, and H. Sowers, Layered Magnetic Structures: Evidence for Antiferromagnetic Coupling of Fe Layers Across Cr Interlayers, Phys. Rev. Lett. **57,** 2442 (1986).

[16] J. C. Slonczewski, Conductance and exchange coupling of two ferromagnets separated by a tunneling barrier, Phys. Rev. B **39,** 6995 (1989).

[17] S. Parkin, N. More, and K. Roche, Oscillations in Exchange Coupling and Magnetoresistance in Metallic Superlattice Structures: Co/Ru, Co/Cr, and Fe/Cr, Phys. Rev. Lett. **64,** 2304 (1990).

[18] P. Bloemen, H. Van Kesteren, H. Swagten, and W. De Jonge, Oscillatory interlayer exchange coupling in Co/Ru multilayers and bilayers, Phys. Rev. B **50,** 13505 (1994).

[19] R. Lavrijsen, A. Fernández-Pacheco, D. Petit, R. Mansell, J. Lee, and R. Cowburn, Tuning the interlayer exchange coupling between single perpendicularly magnetized CoFeB layers, Appl. Phys. Lett. **100,** 052411 (2012).

[20] C.-W. Cheng, C. Shiue, T.-I. Cheng, and G. Chern, Observation of parallel-antiparallel magnetic coupling in ultrathin CoFeB-MgO based structures with perpendicular magnetic anisotropy, J. Appl. Phys. **112,** 033917 (2012).

[21] F. Hooge and A. Hoppenbrouwers, $1/f$ noise in continuous thin gold films, Physica **45,** 386 (1969).

[22] F. N. Hooge, 1/f noise is no surface effect, Phys. Lett. A **29,** 139 (1969).

[23] F. Hooge, Discussion of recent experiments on 1/f noise, Physica **60,** 130 (1972).

[24] D. Mazumdar, X. Liu, B. Schrag, M. Carter, W. Shen, and G. Xiao, Low frequency noise in highly sensitive magnetic tunnel junctions with (001) MgO tunnel barrier, Appl. Phys. Lett. **91,** 033507 (2007).

[25] D. Mazumdar, W. Shen, X. Liu, B. Schrag, M. Carter, and G. Xiao, Field sensing characteristics of magnetic tunnel junctions with (001) MgO tunnel barrier, J. Appl. Phys. **103,** 113911 (2008).

[26] Y. Zhang, G. He, X. Zhang, and G. Xiao, Magnetotransport and electronic noise in superparamagnetic magnetic tunnel junctions, Appl. Phys. Lett. **115,** 022402 (2019).

[27] M. Sampietro, L. Fasoli, and G. Ferrari, Spectrum analyzer with noise reduction by cross-correlation technique on two channels, Rev. Sci. Instrum. **70,** 2520 (1999).

[28] K. Wang, L. Qian, W. Chen, S.-C. Ying, G. Xiao, and X. Wu, Spin torque effect on topological defects and transitions of magnetic domain phases in Ta/CoFeB/MgO, Phys. Rev. B **99,** 184410 (2019).

[29] Y. Haddab, V. Mosser, M. Lysowec, J. Suski, L. Demeus, C. Renaux, S. Adriensen, and D. Flandre, Low-noise SOI Hall devices, Proc. SPIE **5115,** 196 (2003).

[30] M. Behet, J. Bekaert, J. De Boeck, and G. Borghs, $Inas/A_{l0.2}Ga_{0.8}Sb$ quantum well Hall effect sensors, Sens. Actuators, A Phys. **81,** 13 (2000).

[31] J. Jankowski, S. El-Ahmar, and M. Oszwaldowski, Hall sensors for extreme temperatures, Sensors **11,** 876 (2011).

[32] M.-C. Tsai, C.-W. Cheng, C. Tsai, and G. Chern, The intrinsic temperature dependence and the origin of the crossover of the coercivity in perpendicular MgO/CoFeB/Ta structures, J. Appl. Phys. **113,** 17C118 (2013).

[33] K.-M. Lee, J. W. Choi, J. Sok, and B.-C. Min, Temperature dependence of the interfacial magnetic anisotropy in W/CoFeB/MgO, AIP Adv. **7,** 065107 (2017).

[34] H. Sato, P. Chureemart, F. Matsukura, R. Chantrell, H. Ohno, and R. Evans, Temperature-dependent properties of CoFeB/MgO thin films: Experiments versus simulations, Phys. Rev. B **98,** 214428 (2018).

[35] C. Zheng, K. Zhu, S. C. De Freitas, J.-Y. Chang, J. E. Davies, P. Eames, P. P. Freitas, O. Kazakova, C. Kim, and C.-W. Leung, Magnetoresistive sensor development roadmap (non-recording applications), IEEE Trans. Magn. **55,** 1 (2019).

[36] G. He, Y. Zhang, L. Qian, G. Xiao, Q. Zhang, J. C. Santamarina, T. W. Patzek, and X. Zhang, Picotesla magnetic tunneling junction sensors integrated with double staged magnetic flux concentrators, Appl. Phys. Lett. **113,** 242401 (2018).

[37] J. P. Valadeiro, J. Amaral, D. C. Leitão, R. Ferreira, S. F. Cardoso, and P. J. Freitas, Strategies for pTesla field detection using magnetoresistive sensors with a soft pinned sensing layer, IEEE Trans. Magn. **51,** 1 (2015).

[38] E. Paz, S. Serrano-Guisan, R. Ferreira, and P. Freitas, Room temperature direct detection of low frequency magnetic fields in the 100 $pT/Hz_{0.5}$ range using large arrays of magnetic tunnel junctions, J. Appl. Phys. **115,** 17E501 (2014).

[39] S. Cardoso, D. Leitao, L. Gameiro, F. Cardoso, R. Ferreira, E. Paz, and P. Freitas, Magnetic tunnel junction sensors with pTesla sensitivity, Microsyst. Technol. **20,** 793 (2014).

[40] R. Guerrero, M. Pannetier-Lecoeur, C. Fermon, S. Cardoso, R. Ferreira, and P. Freitas, Low frequency noise in arrays of magnetic tunnel junctions connected in series and parallel, J. Appl. Phys. **105,** 113922 (2009).